# Chandra Resolves the T Tauri Binary System RW Aur

Stephen L. Skinner<sup>1</sup>and Manuel Güdel<sup>2</sup>

## **ABSTRACT**

RW Aur is a multiple T Tauri system consisting of an early-K type primary (A) and a K5 companion (B) at a separation of 1."4. RW Aur A drives a bipolar optical jet that is well-characterized optically. We present results of a sensitive Chandra observation whose primary objective was to search for evidence of soft extended X-ray emission along the jet, as has been seen for a few other nearby T Tauri stars. The binary is clearly resolved by *Chandra* and both stars are detected as X-ray sources. The X-ray spectra of both stars reveal evidence for cool and hot plasma. Suprisingly, the X-ray luminosity of the less-massive secondary is at least twice that of the primary and is variable. The disparity is attributed to the primary whose X-ray luminosity is at the low end of the range for classical T Tauri stars of similar mass based on established correlations. Deconvolved softband images show evidence for slight outward elongation of the source structure of RW Aur A along the blueshifted jet axis inside the central arcsecond. In addition, a faint X-ray emission peak is present on the redshifted axis at an offset of  $1.2''\pm0.''2$  from the star. Deprojected jet speeds determined from previous optical studies are too low to explain this faint emission peak as shock-heated jet plasma. Thus, unless flow speeds in the redshifted jet have been underestimated, other mechanisms such as magnetic jet heating may be involved.

Subject headings: stars: individual (RW Aur) — accretion, accretion disks — stars: pre-main sequence — X-rays: stars

# 1. Introduction

RW Aur is a binary system consisting of a pair of classical T Tauri stars (TTS). Their properties are summarized in Table 1. The optically-bright  $\sim$ K1 primary RW Aur A and

<sup>&</sup>lt;sup>1</sup>CASA, Univ. of Colorado, Boulder, CO, USA 80309-0389; stephen.skinner@colorado.edu

<sup>&</sup>lt;sup>2</sup>Dept. of Astrophysics, Univ. of Vienna, Türkenschanzstr. 17, A-1180 Vienna, Austria; manuel.guedel@univie.ac.at

fainter K5 secondary were clearly revealed in K-band speckle images acquired with the Hale 5m Telescope by Ghez, Neugebauer, & Matthews (1993). A third faint component identified as C was also visible in their K-band speckle images at an offset of 0.''12 from B but component C was not confirmed in subsequent HST optical images which leaves its reality in doubt (Ghez, White, & Simon 1997; White & Ghez 2001). Component B lies at a separation of  $1.''397 \pm 0.''026$  from A along P.A. =  $254.6^{\circ} \pm 1.0^{\circ}$  (White & Ghez 2001). Low-amplitude periodic variations in optical spectral features of RW Aur A were reported by Petrov et al. (2001). They argued that these might be due to a low-mass companion in a 2.77 day orbit but they also noted that the periodic variability could be due to non-axisymmetric accretion onto a single star.

Hirth et al. (1994) detected an asymmetric bipolar outflow from RW Aur A using H $\alpha$ and forbidden-line emission long-slit spectra. Follow-up deep imaging in [S II]  $\lambda\lambda6716$ , 6731 by Mundt & Eislöffel. (1998) traced the blueshifted southeastern lobe of the jet-like flow out to more than 100". Even though the blueshifted lobe is more extended the redshifted lobe was found to be brighter within 10" of the star. Their images revealed at least ten knots in the jet. The bright inner redshifted lobe was confirmed in spectacular [S II] and [O I] adaptive optics images obtained in 1997 with the CFHT by Dougados et al. (2000) and in 1998 by López-Martín, Cabrit, & Dougados (2003). Their images traced the redshifted lobe down to separations of <1'' and showed several jet knots including a prominent redshifted knot designated R5 at a separation of 1."07 - 1."32 from the star. They determined the position angle of the inner regions of the blueshifted jet to be P.A. =  $130^{\circ} \pm 2^{\circ}$ . HSTSTIS observations were obtained by Woitas et al. (2002) in which the jet was traced down to within 0."1 of the central source in forbidden emission lines. Their results confirm the radial velocity asymmetry with the outflow velocity of the blueshifted lobe being about 50% larger than the redshifted lobe and suggest that the asymmetry difference is time-variable on timescales of a few years. Further analysis of the HST data by Melnikov et al. (2009) shows evidence for jet knots at separations ranging from <1'' out to  $\approx 3''$  from the star and provides estimates of jet properties (e.g. electron temperature and density, ionization fraction, radial velocity, and jet mass-loss rate).

RW Aur and its jet have been well-studied optically but the availability of modern X-ray telescopes with arcsecond spatial resolution such as Chandra has now opened a new spectral window for jet studies. Jets with outflow speeds of several hundred km s<sup>-1</sup> can produce shocks with temperatures of a few MK capable of emitting soft X-rays. In addition, other processes such as entrained magnetic fields may play a role in heating young stellar jets to X-ray temperatures.

Observational evdidence for X-ray emitting jets in young stars has emerged over the

past decade, but so far only a few examples are known. The best-studied example to date is the classical TTS DG Tau in which faint soft X-ray emission (E < 2 keV) extending outward  $\approx 4''$  - 5" from the star along the jet was seen in high-sensitivity *Chandra* images (Güdel et al. 2005; 2008). Other examples include the optically-revealed stars RY Tau (Skinner, Audard, & Güdel 2011), Z CMa (Stelzer et al. 2009), and HD 163296 (Swartz et al. 2005; Günther, Schneider, & Li 2013) as well as heavily-obscured protostars such as L1551 IRS 5 (Bally, Feigelson, & Reipurth 2003; Schneider, Günther, & Schmitt 2011). The X-ray jet emission from these young stars and protostars is typically faint (tens of counts in exposures of <100 ksec), soft (E < 2 keV), and visible only out to a few arcseconds from the central star.

In order to better characterize the ubiquity and nature of X-ray jet emission from young stars, additional examples of this phenomenon are needed. RW Aur offers a promising candidate for X-ray jet studies because of its proximity (d = 140 pc), low intervening extinction ( $A_v = 0.4 \text{ mag}$ ; Table 1), and well-delineated optical jet which has been traced inward to within  $\approx 1''$  of the star. A previous XMM-Newton observation in 2007 detected RW Aur as an X-ray source (Güdel et al. 2010) but the angular resolution was not sufficient to clearly resolve the close AB pair. We present here a higher spatial resolution Chandra observation of RW Aur which clearly resolves the binary and shows that both stars are X-ray sources. This observation reveals previously unknown X-ray properties of RW Aur A including a faint emission peak lying on the redshifted jet axis near the star that may be jet-related as well as an unusual X-ray spectrum that includes very soft and very hard emission. An unexpected finding is that the less-massive secondary RW Aur B is more luminous in X-rays than the jet-driving primary.

## 2. Chandra Observation

The Chandra observation (ObsId 14539) was carried out on 12 January 2013 from 01:13 - 18:09 TT with an exposure live time of 54,482 s. Exposures were obtained using the ACIS-S (Advanced CCD Imaging Spectrometer) array in FAINT timed-event mode. RW Aur was placed at the nominal aimpoint on the ACIS-S3 CCD which was configured in 1/8 subarray mode. The use of subarray mode restricts the field-of-view to a rectangular region of 128 × 1024 native pixels, or  $\approx 63'' \times 504''$  at the native pixel size of 0."492. Subarray mode was selected in order to use a short 0.4 s frame time that would mitigate photon pileup in the event of a large X-ray flare (no large flares occurred). For an on-axis point source, the ACIS-S 90% encircled energy radius at 1.4 keV is  $R_{90} \approx 0$ ."9. Further information on Chandra and

its instrumentation can be found in the *Chandra* Proposer's Observatory Guide (POG)<sup>3</sup>.

The pipeline-processed data files provided by the Chandra X-ray Center (CXC) were analyzed using standard science threads with CIAO version 4.4<sup>4</sup>. The CIAO processing used recent calibration data from CALDB version 4.4.10. Source events, spectra, and light curves were extracted from circular regions of radii 0."9 centered on the X-ray peaks of A and B. Because of the close 1."4 source separation, the common region between A and B where the two extraction circles overlap was excluded in order to minimize cross-contamination. Background was extracted from nearby source-free regions. Background is negligible, amounting to less than 1 count (0.2 - 8 keV) within the extraction circle during the 54 ks exposure. CIAO specextract was used to extract spectra along with source-specific response matrix files (RMFs) and auxiliary response files (ARFs). Spectral fitting, timing analysis, and image analysis were undertaken with the HEASOFT Xanadu<sup>5</sup> software package (v. 6.12) including XSPEC vers. 12.7.1 and XRONOS vers. 5.2.1. Additional tests for source variabilility were carried out on energy-filtered source event lists using the Bayesian-method CIAO tool glvary (Gregory & Loredo 1992, 1996).

#### 3. Results

Both RW Aur A and B are clearly detected. Their X-ray properties are summarized in Table 2.

### 3.1. Image Analysis

A key motivation for this observation was to determine whether the RW Aur A jet (in addition to the star itself) might be a source of X-rays. We have thus carefully examined the *Chandra* images to discern whether any extension is visible outward along the direction of the optical jet. Based on *Chandra* observations of other jet sources such as DG Tau (Güdel et al. 2005; 2008) and RY Tau (Skinner, Audard, & Güdel 2011) we anticipate that any extended X-ray structure from the jet would be dominated by soft emission with energies E < 2 keV and would be visible out to a few arcseconds from the central source. The redshifted axis

<sup>&</sup>lt;sup>3</sup>See http://asc.harvard.edu/proposer/POG

 $<sup>^4</sup>$ Further information on Chandra Interactive Analysis of Observations (CIAO) software can be found at http://asc.harvard.edu/ciao.

<sup>&</sup>lt;sup>5</sup>http://heasarc.gsfc.nasa.gov/docs/xanadu/xanadu.html.

along P.A. = 310° is of particular interest since optical images show at least six redshifted emission knots at separations of 0."25 - 3."5 from the star (Dougados et al. 2000; Melnikov et al. 2009).

Chandra clearly separates the A and B components as evident from the soft-band (0.2 - 2 keV) image in Figure 1 (without deconvolution). If any significant X-ray extension were present we would expect to see source elongation at offsets of >1'' from the central peak where PSF effects no longer dominate. No such structure is visible but a slight outward elongation of the contours along the blueshifted jet is seen inside the central arcsecond. We find no significant difference between the X-ray centroid position of RW Aur A in the soft (0.2 - 2 keV) and hard (2 - 8 keV) band images.

To search more closely for evidence of extended structure we generated deconvolved soft-band images using the CIAO arestore<sup>6</sup> tool which implements the Lucy-Richardson method (Lucy 1974; Richardson 1972). Deconvolution removes some of the blurring effect due to telescope optics. However, the procedure is not perfect due to several factors including imprecise modeling of the Chandra telescope optics and PSF as well as uncertainties in the energy and off-axis dependence of the PSF. In particular, there is a suspected asymmetry in the Chandra PSF which is not yet taken into account in Chandra PSF simulation tools, as discussed further below. It is also worth noting that the Lucy-Richardson method gives best results for bright point sources whereas the number of counts in the present case is modest, especially for source A (Fig. 1). The deconvolution was performed using an observation-specific image of the Chandra PSF produced using the Chart ray-tracing and MARX simulators as prescribed in CIAO science thread procedures. These procedures take into account the telescope optics as well as the position of the source on the detector and the source spectrum. Event lists provided by CXC now include energy-dependent subpixel event repositioning (EDSER) by default. Since Chandra simulation tools do not yet have the capability to generate EDSER-enhanced PSFs, we removed the EDSER prior to generating simulated PSFs.

Since structure in deconvolved images can be sensitive to the number of iterations applied during the procedure, we generated images using 25, 50, 100, and 200 iterations. Representative deconvolved images in the 0.2 - 2 keV and 0.2 - 1.5 keV energy bands using 100 iterations and the respective PSF images used to produce them are shown in Figure 2. The structure of RW Aur A is now almost completely confined to within a region of radius 0."5 due to mitigation of PSF smearing effects (Fig. 2-top left). Along the blueshifted jet, some weak extension of the central core region out to 0."6 from the peak of source A is visible in

<sup>&</sup>lt;sup>6</sup>http://cxc.harvard.edu/ciao/ahelp/arestore.html

the deconvolved images, as was already noticeable in the raw image without deconvolution (Fig. 1-left). The blueward extension becomes more apparent in the smoothed deconvolved image using the more restrictive 0.2 - 1.5 keV energy cut shown in Figure 2-bottom. No corresponding extension outward from the central source is visible along the redshifted jet, but a faint isolated emission peak is present along the redshifted axis at an offset of 1."2±0.2" from the central peak. This weak feature is also present in images obtained using 50 and 200 iterations and becomes more localized as the number of iterations is increased from 50 to 200. The feature contains 11±2 counts (0.2 - 2 keV), where the uncertainty reflects only the dependence on the number of iterations and is not statistical.

Some caution is needed in interpreting the faint X-ray peak on the redshifted jet axis as a real emission feature. There is a known asymmetry in the Chandra PSF<sup>7</sup> which can produce artificial structure in deconvolved images inside the central arcsecond. The artificial structure is hook-shaped, contains a small fraction of the total flux, and is confined to small offsets of  $0.''6 \le r \le 1''$  from the central source over a range of roll-dependent position angles. The asymmetry does not affect images on scales larger than one arcsecond. For the RW Aur observation the nominal roll angle was ROLL = 272.1° and the affected region lies along P.A. = 282.9° ( $\pm 25^{\circ}$ ), measured from north to east. The sector regions that may be affected by the PSF asymmetry<sup>8</sup> are overplotted in Figure 2 for both the A and B components. We refer to these hereafter as sector A and sector B.

For deconvolved images obtained using  $\geq 50$  iterations, no significant counts are present in sector A but residual counts are clearly present in the sector B. In the deconvolved image in Figure 2-top left (100 iterations; 0.2 - 2 keV), there is <1 count in sector A and  $\approx 41$  counts in sector B. The elongated structure in B does not extend beyond the outer sector boundary at r=1'' and the 41 counts in sector B lie within the lower P.A. range of the sector. On the other hand, the faint feature visible in A lies beyond the outer sector boundary and appears on the redshifted jet axis at the higher P.A. end of sector A. The above differences in the spatial distribution of counts between sources A and B combined with the fact that sector A is free of counts suggests that the weak feature at  $r \approx 1.''2$  along the redshifted jet axis of RW Aur A could be real X-ray emission associated with the jet. In order to confirm this, a follow-up observation obtained at a different roll angle in order to rotate the region affected by the asymmetry away from the redshifted jet axis would be needed.

To make a brief comparison of the deconvolved X-ray images with previous optical

 $<sup>^7</sup> Additional information on the PSF asymmetry can be found at:$  $<math display="block">http://cxc.harvard.edu/ciao/caveats/psf\_artifact.html\ .$ 

<sup>&</sup>lt;sup>8</sup>The sector regions were generated using the CIAO tool make\_psf\_asymmetry\_region .

observations, we note that the 1."2 offset of the X-ray feature from source A is nearly identical to that of the redshifted knot R5 seen in December 1998 CFHT observations (Dougados et al. 2000; López-Martin et al. 2003). However, they find a proper motion of  $\mu = 0$ ."24±0."05 yr<sup>-1</sup> for the R5 knot so the X-ray feature seen in our January 2013 observation cannot be R5. A similar argument applies to redshifted knots J1 (offset 0."25), J2 (0."9), and J3 (1."8) seen in December 2000 HST images (Melnikov et al. 2009) whose proper motions were estimated to be  $\approx 0$ ."2 yr<sup>-1</sup> by Woitas et al. (2002). Based on these proper motions, the above knots would have moved outward  $\approx 2$ ."4 during the  $\approx 12$  years between the HST and Chandra observations. If the faint X-ray peak originates in the jet then it is a new feature that has formed since the previous CFHT and HST observations.

## 3.2. Timing Analysis

Light curves of RW Aur A and B are shown in Figure 3. The CIAO glvary tool gives a probablility of constant count rate  $P_{const} = 0.96$  (0.2 - 8 keV) for RW Aur A, so no significant variability was detected in the primary star. On the other hand, a similar test for RW Aur B gives  $P_{const} < 0.001$  (0.2 - 8 keV) so variability is present. As the light curves in Figure 2 show, the broad-band count rate of B increased by  $\approx 30\%$  in the second half of the observation. This increase is most clearly seen in the hard 2 - 8 keV band. A slight increase in the soft band (0.2 - 2 keV) count rate is also seen, but no variability was detected in the softest emission in the 0.2 - 1 keV range. The increase in count rate of component B was accompanied by a flux increase (Sec. 3.3.2) and a hardness increase. During the first half of the observation the median photon event energy of B was  $E_{50} = 1.07$  keV and during the second half it was  $E_{50} = 1.17$  keV. The corresponding mean photon energies were  $\overline{E} = 1.29$  keV and 1.45 keV.

## 3.3. Spectral Analysis

The spectra of RW Aur A and B are shown in Figure 4. Spectral fits using absorbed optically-thin plasma models require two temperature components (2T) to obtain acceptable fits as measured by  $\chi^2$  statistics. In the case of RW Aur A we also consider a hybrid model consisting of a cool isothermal plasma (1T) plus a power-law to reproduce the emission at higher energies. Fit results are given in Table 3.

### 3.3.1. RW Aur A

The best-fit X-ray absorptions toward both A and B are quite low. In the case of RW Aur A the absorption is so low that the value of the column density  $N_H$  cannot be accurately determined from the X-ray spectrum because of the rapid falloff in ACIS-S sensitivity at energies below 0.5 keV. Based on spectral fits we derive an upper 90% confidence bound  $N_H = 6.5 \times 10^{20}$  cm<sup>-2</sup>. Table 3 includes a fit in which  $N_H$  was allowed to vary as well as fits in which it was held fixed at the upper 90% confidence bound. The above upper limit corresponds to  $A_V = 0.3$  mag using the  $N_H$  to  $A_V$  conversion of Gorenstein (1975) or  $A_V = 0.4$  mag using the conversion of Vuong et al. (2003). These values are consistent with the extinction obtained in ground-based observations by White & Ghez (2001), namely  $A_v = 0.39\pm0.33$  or equivalently  $A_V = 0.35\pm0.30$  mag.

The spectrum of RW Aur A has some noteworthy features. High-temperature lines are visible including the blended He-like triplets Mg XI (1.35 keV;  $\log T_{max} = 6.8$ ), Si XIII (1.86 keV;  $\log T_{max} = 7.0$ ), and S XV (2.46 keV;  $\log T_{max} = 7.2$ ) where  $T_{max}$  (K) is the maximum line-power temperature. Thus, there is little doubt that hot plasma (T  $\gtrsim 10$  MK) is present in the spectrum. Even so, spectral fits with multi-temperature thermal models do not tightly constrain the temperature of the hot plasma. Our models are only able to constrain the 90% confidence lower bound which is  $kT_2 \geq 20 \text{ keV}$  if the spectra are rebinned to a minimum of 10 counts per bin (Table 3) or  $kT_2 \ge 16$  keV if rebinned to 20 counts per bin. The high temperature component is present even in spectra extracted using circular regions as small as r = 0."3 centered on RW Aur A. Of the 986 broad-band counts (0.2 - 8 keV) detected in RW Aur A, 50 (5.1%) are in the high-energy 4 - 8 keV range and we estimate no more than 3 of these 50 are due to contamination from RW Aur B. By comparison, RW Aur B has 2909 broad-band counts of which 70 (2.4%) are in the high-energy 4 - 8 keV range. The very high temperature of RW Aur A is somewhat unusual since hot-component plasma temperatures in T Tauri stars in the absence of large flares are typically less than  $\sim 5$  keV. The inability to tightly constrain the hot-component temperature is due at least in part to the limited number of counts in the very hard 4 - 8 keV band.

Because of the apparent very high plasma temperature inferred from 2T thermal models we also tried to fit the spectrum of RW Aur A with a composite model consisting of a cool thermal plasma plus a power-law (PL) to reproduce the hard continuum. The physical relevance of a PL model is questionable since TTS X-ray spectra are usually well-fitted with thermal models. Nevertheless, the hybrid 1T+PL model provides a slightly better fit to the spectrum as measured by  $\chi^2$  statistics than does the 2T thermal model (Table 3). In this composite model the thermal component accounts for almost all of the observed emission below 2.5 keV and the power-law reproduces the hard featureless emission at higher energies

(Fig. 5). The power-law spectrum is nearly flat with a photon power-law index  $\Gamma_{ph} = -0.04$  [-0.76 - +0.59].

The 2T and 1T +PL models give similar X-ray luminosities of log  $L_x = 29.44 - 29.51$  (ergs s<sup>-1</sup>) for RW Aur A. We compare these values with predictions based on known correlations between  $L_x$  and stellar mass and luminosity in Section 4.2.

## 3.3.2. RW Aur B

There are sufficient counts in the Chandra spectrum of RW Aur B to reliably determine a best-fit value of  $N_H$  (as opposed to only an upper limit). The 2T model in Table 3 in which  $N_H$  was allowed to vary gives  $N_H = 4.3 \ [2.3 - 6.5] \times 10^{20} \ cm^{-2}$  where brackets enclose the 90% confidence range. This equates to  $A_V = 0.20 \ [0.10 - 0.30]$  (Gorenstein et al. 1975) or  $A_V = 0.27 \ [0.14 - 0.41]$  (Vuong et al. 2003). These values suggest low absorption similar to that of RW Aur A and agree with the value  $A_V = 0.32 \pm 0.11$  for RW Aur B given in Ghez et al. (1997). However, this value is significantly less than  $A_v = 1.56 \pm 0.24$  ( $A_V = 1.40 \pm 0.22$ ) obtained by White & Ghez (2001). For completeness, we have thus included a fit of RW Aur B in Table 3 holding the absorption fixed at  $N_H = 2.24 \times 10^{21} \ cm^{-2}$  corresponding to  $A_V = 1.40$  using the Vuong et al. (2003) conversion. This higher absorption fit yields slightly lower plasma temperatures and higher  $L_x$ . The reduced  $\chi^2$  value is greater than for the low-absorption fit but is still marginally acceptable.

The X-ray spectrum of RW Aur B is quite typical of a cTTS. Hot plasma at  $kT_2 \approx 2$  - 3 keV is present as revealed by Mg XI, Si XIII, and S XV features in the spectrum (Fig. 3-top). The count rate increased during the second half of the observation and the emission became slightly harder as gauged by a change in the hardness ratio (H.R.; Table 2) from H.R. = -0.79 in the first half to -0.68 in the second half.

To search for changes in the spectrum of RW Aur B, we extracted and fitted separate spectra for the first half (1246 counts) and second half (1663 counts) of the observation. The spectra were fitted with an absorbed 2T thermal plasma model and the absorption was held fixed at the best-fit value  $N_{\rm H} = 4.3 \times 10^{20}~{\rm cm}^{-2}$  determined from the spectral fit for the full exposure (Table 3). Fixing the value of  $N_{\rm H}$  is justified since any significant change in  $N_{\rm H}$  would have resulted in different count rates at very low energies <0.5 keV between the first and second halves, but no significant change was observed.

Fits of the spectra for the first and second halves show no significant change in the temperature of the cool component ( $kT_1$ ). In contrast, a modest increase in the temperature of the hot plasma component from  $kT_2 = 2.87$  [2.04 - 6.38, 90% conf.] keV to  $kT_2 = 3.40$ 

[2.72 - 5.33] keV is inferred. The broad-band flux (0.2 - 8 keV) increased by  $\approx 43\%$  during the second half of the observation (Table 3 notes). The unabsorbed flux of RW Aur B during the first half was a factor of  $\sim 2$  greater than that of RW Aur A and a factor of  $\sim 3$  greater in the second half. Assuming A and B lie at the same distance this implies that the secondary is more luminous in X-rays than the primary.

### 4. Discussion

## 4.1. X-ray Jet Emission?

In general, the conditions for detecting X-ray jet emission are more favorable in the approaching blueshifted jet because of lower line-of-sight absorption, but faint X-ray emission in both the redshifted and blueshifted jets of the TTS DG Tau has been detected (Güdel et al. 2005; 2008). Also, RW Aur is somewhat unusual in that its redshifted jet is optically much brighter in regions close to the star than the blueshifted jet (Fig. 1 of Dougados et al. 2000). Given the above, it is worthwhile to consider whether the faint X-ray peak along the redshifted jet axis at an offset of  $\approx 1.$ "2 from RW Aur A might originate in the jet.

One possibility is that the faint X-ray feature is shock-heated plasma in the jet. The predicted temperature for a shock-heated jet with a shock speed  $v_s$  is (Raga et al. 2002)  $T_s = 0.15 \ (v_s/100 \ \text{km s}^{-1})^2 \ \text{MK}$ . The spatially-resolved forbidden emission line data from the HST STIS observations (Melnikov et al. 2009) give a radial velocity for the redshifted jet at an offset of  $\approx 1.''2$  from the star of  $v_r \approx 100 \ \text{km s}^{-1}$ . In fact they find little change in the radial velocity out to offsets of  $\approx 3''$ . Using the jet inclination angle relative to the line-of-sight of  $i = 46^{\circ} \pm 3^{\circ}$  (López-Martin et al. 2003) the deprojected jet velocity is  $v_{jet} \approx 144 \pm 8 \ \text{km s}^{-1}$ . Adopting the upper limit of this range and assuming the jet impacts a stationary target ( $v_s \approx v_{jet} \approx 152 \ \text{km s}^{-1}$ ), then the maximum shock temperature is  $T_s \approx 0.35 \ \text{MK}$  ( $kT_s \approx 0.03 \ \text{keV}$ ). This temperature is at least a factor of  $\sim 4$  lower than that needed to produce detectable thermal X-ray emission at  $kT \approx 0.1 - 0.2 \ \text{keV}$  ( $T \approx 1 - 2 \ \text{MK}$ ), below which Chandra has little sensitivity.

As an additional check, the predicted intrinsic X-ray luminosity of a bow shock is (Raga et al. 2002)

$$L_{jet} = C_o \left[ \frac{n_o}{100 \text{ cm}^{-3}} \right]^{\alpha} \left[ \frac{r_{bs}}{10^{16} \text{ cm}} \right]^{\beta} \left[ \frac{v_s}{100 \text{ km s}^{-1}} \right]^{\gamma} L_{\odot}$$
 (1)

where  $n_o$  is the preshock number density,  $r_{bs}$  is the characteristic radius of the bow shock around its axis, and  $v_s$  is the shock speed. For the case of a radiative shock:  $C_o = 4.1 \times 10^{-6}$ ,  $\alpha = 1$ ,  $\beta = 2$ ,  $\gamma = 5.5$ . For the nonradiative case:  $C_o = 4.5 \times 10^{-5}$ ,  $\alpha = 2$ ,  $\beta = 3$ ,  $\gamma = 1$ . Optical observations of the redshifted jet of RW Aur at an offset of 1."2 from the star give  $n_o \approx 1585$  cm<sup>-3</sup> (Melnikov et al. 2009) and FWHM  $\approx 28$  AU (Dougados et al. 2000; Woitas et al. 2002). Taking  $r_{bs} = 14$  AU (i.e. the jet half-width) and assuming  $v_s \approx 150$  km s<sup>-1</sup> as above, the radiative case gives  $L_{jet,r} = 1 \times 10^{26}$  ergs s<sup>-1</sup> and for the nonradiative case  $L_{jet,nr} = 6 \times 10^{24}$  ergs s<sup>-1</sup>. Assuming that the weak  $\approx 11$  count X-ray peak is a thermal source seen through negligible absorption its intrinsic X-ray luminosity is  $L_x = 3 \times 10^{27}$  ergs s<sup>-1</sup> assuming kT = 0.2 keV or  $L_x = 2 \times 10^{27}$  ergs s<sup>-1</sup> assuming kT = 0.5 keV. These  $L_x$  values are at least an order of magnitude greater than predicted above for a shocked jet.

The above comparisons show that the faint X-ray peak is not compatible with emission from a shocked jet knot unless the redshifted jet (shock) velocity is significantly greater than determined from previous optical data. In order to reconcile the X-ray emission with a shock interpretation one would need to postulate the existence of optically-undetected jet material moving at speeds in excess of  $v_{jet} \sim 300 \text{ km s}^{-1}$  or a jet inclination angle  $i > 70^{\circ}$ . Even though deprojected speeds in the blueshifted jet may approach  $-275 \text{ km s}^{-1}$  assuming the nominal jet inclination  $i = 46^{\circ}\pm3^{\circ}$  (Melnikov et al. 2009), there is presently no firm evidence for such high speeds in the redshifted jet or for a jet inclination  $> 70^{\circ}$ . Thus, based on existing data, a shock origin for the faint X-ray peak seems unlikely and other explanations must be considered.

If the jet is threaded by a weak magnetic field such as detected in the HH 80-81 jet (Carrasco-González et al. 2010), then shock-heating could be augmented by magnetic heating to achieve X-ray temperatures. Another possible mechanism for attaining higher outflow speeds and X-ray emitting temperatures is via plasmoid ejections (Hayashi et al. 1996). Using published mass and radius estimates for RW Aur A (Table 1), the escape speed from its surface is  $v_{esc} \approx 560 \text{ km s}^{-1}$  so any ejected plasmoid would be moving at speeds sufficient to produce soft X-ray emission via shocks or even intrinsic thermal X-ray emission if the plasmoid is hot enough (T  $\gtrsim 10^7 \text{ K}$ ). Further discussion of the plasmoid hypothesis can be found in Skinner et al. (2011).

## 4.2. X-ray Luminosity Disparity

As noted above, the less-massive component RW Aur B is  $\sim 2$  - 3 times more X-ray luminous than RW Aur A. This is contrary to expectations since  $L_x$  is correlated with stellar mass  $M_*$  and stellar luminosity  $L_*$  in TTS. The reason for the correlation is not well-understood

but it has been documented in large nearly-coeval samples of TTS in Taurus (Telleschi et al. 2007) and in the Orion Nebula Cluster (Preibisch et al. 2005). For the Taurus cTTS sample studied by Telleschi et al., which is relevant here, their regression fit using the parametric estimation maximization method gives  $\log L_x = (1.70\pm0.20)\log(M_*/M_{\odot}) + 30.13\pm0.09$ . For the stellar luminosity correlation they obtain  $\log L_x = (1.16\pm0.09)\log(L_*/L_{\odot}) + 29.83\pm0.06$ .

Adopting  $M_* = 1.34 \pm 0.18 M_{\odot}$  for RW Aur A (White & Ghez 2001), the above relation predicts  $\log L_x = 30.35$  (30.14 - 30.66), where the range in parentheses here and below takes into account both the uncertainties in the regression fit and  $M_*$ . The lower value  $M_* = 0.9 M_{\odot}$  from Ingleby et al. (2013) gives  $\log L_x = 30.05$  (29.95 - 30.25). Both of the above estimates are higher than the observed value  $\log L_x = 29.4$  - 29.5 but the estimate for the smaller mass  $M_* = 0.9 M_{\odot}$  is in better agreement with the X-ray data. Thus, either the X-ray luminosity of RW Aur A is at the low end of the expected range for cTTS of similar mass (the scatter is large; see Fig. 1 of Telleschi et al. 2007) or its mass has been slightly overestimated. A similar calculation based on  $L_*$  yields good agreement with the observed  $L_x$  for the lower stellar luminosity  $L_* = 0.5 L_{\odot}$  given by Ingleby et al. (2013). Likewise, reasonably good agreement is obtained with the correlation predictions for RW Aur B if the lower limits on its  $M_*$  and  $L_*$  are adopted (Table 1; White & Ghez 2001).

#### 4.3. Accretion Shocks

Material accreting onto the star can produce soft X-rays in shock-heated plasma at temperatures of a few MK. Soft emission below 0.5 keV is present in the spectrum of RW Aur A (Fig. 4 bottom) with 22 counts detected with energies E < 0.5 keV. Since RW Aur A is accreting at a rate of  $\dot{M}_{acc} \approx 2 \times 10^{-8} \ {\rm M}_{\odot} \ {\rm yr}^{-1}$  (Ingleby et al. 2013), we provide a brief comparison of accretion shock estimates with the observed X-ray properties.

The predicted temperature of the post-shock plasma is (Ingleby et al. 2013)

$$T_{s,acc} = 8.6 \times 10^5 \left[ \frac{M_*}{0.5 M_{\odot}} \right] \left[ \frac{R_*}{2 R_{\odot}} \right]^{-1} K.$$
 (2)

Taking  $M_* = 0.9 M_{\odot}$  and  $R_* = 1.1 R_{\odot}$  (Table 1) the above gives  $T_{s,acc} = 2.8$  MK or kT = 0.24 keV. The intrinsic (unabsorbed) emission of a thermal plasma at this temperature occurs mostly at E < 1 keV with the flux peaking near 0.65 keV. Thus, some of the soft emission detected in RW Aur A may be accretion-related.

We have simulated an accretion shock contribution using a 3T vapec model. This model is identical to the 2T model in Table 3 with  $N_H$  held fixed except that an additional very cool component at a fixed temperature  $kT_{acc} = 0.24$  keV has been added to simulate an

accretion shock. The emission measure (norm) of this component was allowed to vary. The 3T fit converges to values very similar to those of the 2T model and the accretion component contribution is small. Specifically,  $F_x$ ,  $acc(0.2 - 8 \text{ keV}) = 1.42 (2.35) \times 10^{-15} \text{ ergs cm}^{-2} \text{ s}^{-1}$  where the unabsorbed value in parentheses gives  $\log L_{x,acc} = 27.74 \text{ ergs s}^{-1}$ . The simulated accretion component contributes only  $\approx 15 \text{ soft counts}$  (E  $\leq 1 \text{ keV}$ ) to the observed spectrum and its associated  $L_x$  is much less than the total accretion luminosity  $L_{acc} \sim (GM_*\dot{M}_{acc})/R_* \sim 10^{33} \text{ ergs s}^{-1}$ .

## 5. Summary

The main results of this study are the following:

- 1. Chandra has detected X-ray emission from RW Aur A and its companion RW Aur B. The companion is more luminous in X-rays and its emission is variable. Both stars show cool and hot plasma in their spectra. In order to reproduce the hot component of RW Aur A, either a very high temperature thermal plasma or a power-law continuum is required. An accretion shock could be responsible for a small fraction of the coolest emission in RW Aur A at E < 1 keV.
- 2. Deconvolved soft-band images show slight X-ray extension in the source structure of RW Aur A along the blueshifted jet axis close to the star. In addition, deconvolved images reveal a faint X-ray emission peak lying 1."2 ± 0."2 from the star along the redshifted jet axis. This X-ray peak is located at an offset where an optical emission knot was previously observed and it lies outside the region that can be affected by artificial PSF-related structure. As such, the X-ray peak may be real emission associated with the redshifted jet but since the emission is faint a Chandra observation acquired at a different roll angle is needed for confirmation. A comparison with shock models shows that this peak is unlikely to be due to shock-heated jet plasma unless the redshifted jet speed is substantially higher than determined from previous optical observations. Other mechanisms may thus be at work such as magnetic jet heating or plasmoid ejections.
- 3. The X-ray luminosity of RW Aur A is significantly less than predicted based on its published mass range (Table 1) and a known correlation  $L_x \propto M_*$  in TTS. This suggests that  $L_x$  for RW Aur A is at the low end of the range for cTTS of similar mass (the scatter for a given mass is large) or that its mass has been slightly overestimated. The predicted  $L_x$  for RW Aur A based on a correlation with stellar luminosity agrees well

with the observed  $L_x$  if  $L_* \approx 0.5 L_{\odot}$ . For RW Aur B, satisfactory agreement between the observed  $L_x$  and correlation predictions is obtained.

This work was supported by *Chandra* award GO3-14007X issues by the Chandra X-ray Observatory Center (CXC). The CXC is operated by the Smithsonian Astrophysical Observatory (SAO) for, and on behalf of, the National Aeronautics Space Administration under contract NAS8-03060.

## REFERENCES

Anders, E., & Grevesse, N. 1989, Geochim. Cosmochim. Acta, 53, 197

Bally, J., Feigelson, E., & Reipurth, B. 2003, ApJ, 584, 843

Carrasco-González, C., Rodriguez, L.F., Anglada, G., Martí, J., Torrelles, J.M., & Osorio, M. 2010, Science, 330, 1209

Dougados, C., Cabrit, S., Lavalley, C., & Ménard, F. 2000, A&A, 357, L61

Furlan, E. et al. 2011, ApJS, 195, 3

Ghez, A.M., Neugebauer, G., & Matthews, K. 1993, AJ, 106, 2005

Ghez, A.M., White, R.J., & Simon, M. 1997, ApJ, 490, 353

Gorenstein, P., 1975, ApJ, 198, 95

Gregory, P.C., & Loredo, T.J., 1992, ApJ, 398, 146

Gregory, P.C., & Loredo, T.J., 1996, ApJ, 473, 1059

Güdel, M. et al. 2010, A&A, 519, A113

Güdel, M., Skinner, S.L., Audard, M., Briggs, K., & Cabrit, S. 2008, A&A, 478, 797

Güdel, M., Skinner, S.L., Briggs, K.R., Audard, M., Arzner, K., & Telleschi, A. 2005, ApJ, 626, L53

Günther, H.M., Schneider, P.C., & Li, Z.-Y. 2013, A&A, 552, 142

Hayashi, M.R., Shibata, K., & Matsumoto, R. 1996, ApJ, 468, L37

Hirth, G.A., Mundt, R., Solf, J., & Ray, T.P. 1994, ApJ, 427, L99

Ingleby, L. et al. 2013, ApJ, 767, 112

López-Martin, L., Cabrit, S., & Dougados, C. 2003, A&A, 405, L1

Lucy, L.B. 1974, AJ, 79, 745

Melnikov, S.Y., Eislöffel, J., Bacciotti, F., Woitas, J., & Ray, T.P. 2009, A&A, 506, 763

Mundt, R. & Eislöffel, J. 1998, AJ, 116, 860

Petrov, P.P. et al. 2001, A&A, 369, 993

Preibisch, T. et al. 2005, ApJS, 160, 401

Raga, A.C., Noriega-Crespo, A., & Veláquez, P.F. 2002, ApJ, 576, L149

Richardson, W.H. 1972, J. Opt. Soc. Am., 62, 55

Schneider, P.C., Günther, H.M., & Schmitt, J.H.M.M. 2011, A&A, 530, A123

Skinner, S.L., Audard, M., & Güdel, M. 2011, ApJ, 737, 19

Stelzer, B., Hubrig, S., Orlando, S., Micela, G., Mikulášek, Z., & Schöller, M. 2009, A&A, 499, 529

Swartz, D.A. et al. 2005, ApJ, 628, 811

Telleschi, A., Güdel, M., Briggs, K.R., Audard, M., & Palla, F. 2007, A&A, 468, 425

Vuong, M.H., Montmerle, T., Grosso, N., Feigelson, E.D., Verstraete, L., & Ozawa, H. 2003, A&A, 408, 581

White, R.J. & Ghez, A.M. 2001, ApJ, 556, 265

Woitas, J., Ray, T.P., Bacciotti, F., Davis, C.J., & Eislöffel, J. 2002, ApJ, 580, 336

This preprint was prepared with the AAS IATEX macros v5.0.

Table 1. Properties of RW Aur

Object	Туре	log Age (y)	$_{({ m M}_{\odot})}^{{ m M}_{st}}$	$R_*$ $(R_{\odot})$	$T_{eff}$ (K)	$\log L_* \ (L_{\odot})$	$A_v$ (mag)	d (pc)	Refs.
RW Aur A	К3		0.9	1.1		-0.30	0.55	140	1,2
RW Aur A	$K1\pm2$	$6.92 {\pm} 0.31$	$1.34 {\pm} 0.18$		5082	$0.23 \pm 0.14$	$0.39 \pm 0.33$	140	3
RW Aur B	K5	$7.13 {\pm} 0.18$	$0.93 {\pm} 0.09$		4395	$-0.40 \pm 0.10$	$1.56 {\pm} 0.24$	140	3

Note. —  $A_v = 1.11 A_V$ .

Table 2. X-ray Properties of RW Aur (Chandra ACIS-S)

Name	R.A. (J2000)	decl. (J2000)	Net Counts (cts)	H.R.	${\rm E}_{50} \ {\rm (keV)}$	$P_{const}$	$\log L_x $ (ergs s <sup>-1</sup> )	2MASS Identification(offset) (arcsec)
RW Aur A RW Aur B	05 07 49.54 05 07 49.43	+30 24 04.95 +30 24 04.55	$986 \pm 33$ $2909 \pm 33$	-0.72 $-0.73$	1.00 1.12	0.96 <0.001	29.44 29.89	J050749.538+302405.07 (0.12)

Note. — The nominal pointing position for the observation was (J2000.0) RA =  $05^h$   $07^m$  50.33 $^s$ , decl. =  $+30^\circ$  23′ 59″.7. X-ray data are from CCD7 (ACIS chip S3) using events in the 0.2 - 8 keV range inside a circular source extraction region of radius 0″.9 centered on the X-ray peak of each star. Events common to both sources (33 events) where the two circles overlap are excluded. Tabulated quantities are: J2000.0 X-ray position (R.A., decl.), total source counts accumulated in a 54,482 s exposure, hardness ratio H.R. = (H-S)/(H+S) where H = counts(2-8 keV) and S = counts(0.2 - 2 keV), median photon energy (E<sub>50</sub>), probability of constant count-rate determined by the Gregory-Loredo algorithm (P<sub>const</sub>); unabsorbed X-ray luminosity (0.3 - 8 keV at d = 140 pc; L<sub>x</sub> is model-dependent, see Table 3), and 2MASS near-IR counterpart identification. The offset (in parenthesis) is given in arc seconds between the X-ray and 2MASS counterpart position. The X-ray offset of B from A is 1.″48 along P.A. = 254.3°.

<sup>1.</sup> Ingleby et al. (2013). Their value  $A_V=0.5$  ( $A_v=0.55$ ) is based on  $A_J=0.14$  from Furlan et al. (2011), which in turn is based on  $A_v=0.39$  from White & Ghez (2001).

<sup>2.</sup> Furlan et al. (2011)

<sup>3.</sup> White & Ghez (2001).  $A_v$  is from spectral type and  $V - I_C$  color.

Table 3. Chandra Spectral Fits of RW Aur A and B

Parameter					
Object	RW Aur A	RW Aur A	RW Aur A	RW Aur B	RW Aur B
$Model^a$	$2T^{a}$	$2T^{a}$	$1T + PL^{b}$	$2T^{a}$	$2T^{a}$
$N_{\rm H} \ (10^{20} \ {\rm cm}^{-2})$	0.89 [0.00 - 6.50]	$\{6.5\}^{c}$	$\{6.5\}^{c}$	4.3 [2.3 - 6.5]	$\{22.4\}^{d}$
$kT_1 \text{ (keV)}$	0.73 [0.61 - 0.81]	0.65 [0.58 - 0.75]	0.73 [0.64 - 0.79]	0.98 [0.82 - 1.01]	0.39 [0.35 - 0.42]
$kT_2 \text{ (keV)}$	>20.e	$\{20.\}^{f}$		3.15 [2.58 - 4.06]	2.39 [2.09 - 2.74]
$\Gamma_{ph}$			-0.04 [-0.76 - 0.59]		
$norm_1 (10^{-5})^g$	2.71 [1.89 - 3.86]	3.30 [2.46 - 4.15]	5.03 [4.14 - 5.84]	6.80 [4.35 - 9.85]	14.0 [11.4 - 16.8]
$norm_2 (10^{-5})^g$	3.56 [2.61 - 4.25]	2.86 [2.29 - 3.42]	0.10 [0.03 - 0.26]	13.3 [11.1 - 15.3]	18.4 [16.8 - 19.9]
Ne	1.39 [0.10 - 3.00]	1.53 [0.72 - 2.6]	0.76 [0.00 - 1.59]	1.69 [0.09 - 3.30]	2.16 [1.73 - 2.69]
Fe	0.41 [0.29 - 0.60]	0.39 [0.29 - 0.57]	0.27 [0.21 - 0.35]	0.36 [0.24 - 0.50]	0.22 [0.14 - 0.33]
$\chi^2/\mathrm{dof}$	78.5/62	83.3/64	68.9/63	116.1/124	137.4/125
$\chi^2_{red}$	1.27	1.30	1.09	0.94	1.10
$F_X (10^{-13} \text{ ergs cm}^{-2} \text{ s}^{-1})$	1.03(1.06)	0.97(1.17)	1.19(1.39)	$2.93 (3.31)^{h}$	2.75(5.16)
$F_{X,1} (10^{-13} \text{ ergs cm}^{-2} \text{ s}^{-1})$	0.53 (0.55)	$0.51 \ (0.67)$	0.64 (0.83)	1.08(1.27)	0.96(2.55)
$F_{X,2} (10^{-13} \text{ ergs cm}^{-2} \text{ s}^{-1})$	0.50(0.51)	0.46 (0.50)	$0.55 \ (0.56)$	1.85(2.04)	1.79(2.61)
$\log L_X \text{ (ergs s}^{-1}\text{)}$	29.39	29.44	29.51	29.89	30.08
$\log \left[ L_{\rm X}/L_{*} \right]$	-3.89	-3.84	-3.77	-3.29	-3.10

Note. — Based on XSPEC (vers. 12.7.1) fits of the background-subtracted ACIS-S spectra binned to a minimum of 10 counts per bin using 54,482 sec of exposure time. The spectra were modeled with an absorbed two-temperature (2T) vapec optically thin plasma model or an absorbed one-temperature (1T) vapec plasma + a power-law (PL) component. The Ne and Fe abundances were allowed to vary during the fit but their abundances in the cool and hot thermal plasma components were constrained to be equal. The tabulated parameters are absorption column density (N<sub>H</sub>), plasma energy (kT), photon power-law index ( $\Gamma_{ph}$ ), XSPEC component normalization (norm), neon (Ne) and iron (Fe) abundances. Abundances are referenced to the solar values of Anders & Grevesse (1989). Square brackets enclose 90% confidence intervals. Quantities enclosed in curly braces were held fixed during fitting. The total X-ray flux (F<sub>X</sub>) and fluxes associated with each model component (F<sub>X,i</sub>) are the absorbed values in the 0.3 - 8 keV range, followed in parentheses by unabsorbed values. The total X-ray luminosity L<sub>X</sub> is the unabsorbed value in the 0.3 - 8 keV range and assumes a distance of 140 pc. The adopted stellar luminosities are L<sub>\*</sub> = 0.5 L<sub>\infty</sub> for RW Aur A (Ingleby et al. 2013) and L<sub>\*</sub> = 0.4 L<sub>\infty</sub> for RW Aur B (White & Ghez 2001).

 $<sup>^{\</sup>mathrm{a}}\mathrm{XSPEC}$  model of form  $wabs \cdot (vapec + vapec)$  .

 $<sup>{}^{\</sup>rm b}{\rm XSPEC}$  model of form  $wabs{\cdot}(vapec\,+\,pow)$  .

 $<sup>^{\</sup>rm c}{\rm Held}$  fixed during fitting at upper 90% confidence bound.

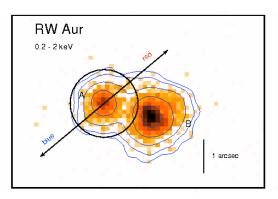
<sup>&</sup>lt;sup>d</sup>Held fixed during fitting at the value inferred from  $A_V = 1.4$  mag ( $A_v = 1.56$ ; White & Ghez 2001) and the  $A_V$  to  $N_H$  conversion of Vuong et al. (2003).

<sup>&</sup>lt;sup>e</sup>Lower 90% confidence bound. Hot-component temperature is poorly-constrained.

 $<sup>^{\</sup>rm f}{\rm Value}$  held fixed during fitting at lower 90% confidence bound.

gFor thermal vapec models, the norm is related to the volume emission measure (EM =  $n_e^2$ V) by EM =  $4\pi 10^{14} d_{cm}^2 \times \text{norm}$ , where  $d_{cm}$  is the stellar distance in cm. At d = 140 pc this becomes EM =  $2.35 \times 10^{56} \times \text{norm}$  (cm<sup>-3</sup>).

<sup>&</sup>lt;sup>h</sup>The flux is variable. The 0.3 - 8 keV fluxes during the first and second halves of the observation in units of  $10^{-13}$  ergs cm<sup>-2</sup> s<sup>-1</sup> were  $F_X = 2.33$  (2.65) and  $F_X = 3.48$  (3.90) where the value in parentheses is unabsorbed. The corresponding X-ray luminosities are  $L_x = 29.79$  and 29.96 (ergs s<sup>-1</sup>).



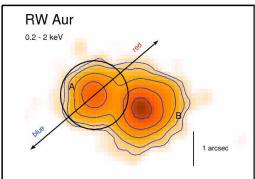


Fig. 1.— Soft-band (0.2 - 2 keV) ACIS-S image of RW Aur generated using 0."125 subpixels and log intensity scale. No deconvolution. The solid black circle around component A has radius = 1". In the 0.2 - 2 keV range, source A has 876 events and B has 2536 events based on circular extraction regions of radius = 0.9" centered on each source. Of these, 24 events lie in the region where the two extraction circles overlap. Arrows show the bipolar optical jet direction along P.A. =  $130^{\circ}/310^{\circ}$ . Slight extension of the outer contours is visible along the blueshifted jet axis. Left: Unsmoothed. Right: Gaussian-smoothed using a 3-subpixel kernel.

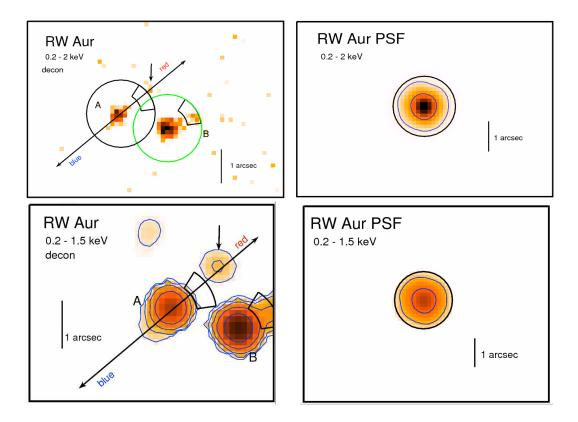


Fig. 2.— Top Left: Deconvolved unsmoothed soft-band (0.2 - 2 keV) ACIS-S image of RW Aur with 0."125 subpixels generated using the Lucy-Richardson method as implemented in the CIAO task arestore (100 iterations). The deconvolution was centered on the brighter source B using the PSF in the right panel. Log intensity scale. The sector regions (PA =  $283^{\circ} \pm 25^{\circ}$ ; radius  $0.6'' \le r \le 1''$ ) may contain artificial structure due to a known PSF asymmetry. There is <1 count in sector A and  $\approx$ 41 counts in sector B. The arrow marks a faint emission peak ( $11\pm 2$  counts) on the redshifted jet-axis of RW Aur A at an offset of 1."2  $\pm$  0."2 from the star. Top Right: Chandra PSF image (0.2 - 2 keV; Gaussian-smoothed; log intensity scale), generated using RW Aur B spectrum as input (Fig. 4). Inner contour is half-maximum, outer contour is 10% maximum. Outer circle has radius 1". Bottom Left: Same as top-left panel except using a more restrictive 0.2 - 1.5 keV energy cut and Gaussian-smoothed with a 3-subpixel kernel. RW Aur A contours are at levels of (0.3, 1.5, 6, 25)% of maximum. Note slight outward extension along blueshifted jet axis. Bottom Right: Same as top-right panel except 0.2 - 1.5 keV.

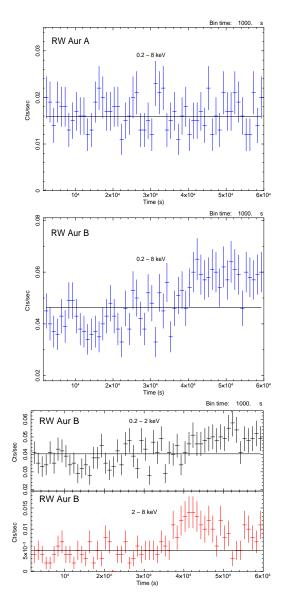


Fig. 3.— Chandra ACIS-S light curves of RW Aur binned at 1000 s intervals. The light curves were extracted from circular regions of radii 0."9 centered on each source but events within the region between the stars where the circles overlap were excluded. Solid horizontal lines show mean count rates. *Top*: RW Aur A (0.2 - 8 keV). No significant variability is detected. *Middle*: RW Aur B (0.2 - 8 keV); variability is clearly present in the second half of the observation. *Bottom*: RW Aur B soft (0.2 - 2 keV) and hard (2 - 8 keV).

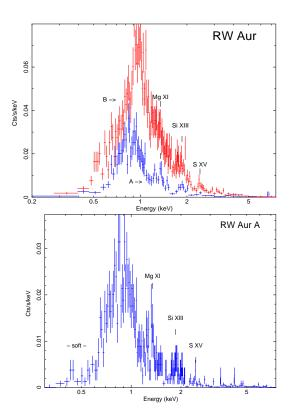


Fig. 4.— Top: Chandra ACIS-S spectra of RW Aur A and B binned to a minimum of 10 counts per bin. The spectra were extracted from circular regions of radii 0."9 centered on each source but events within the region between the stars where the circles overlap were excluded. Possible blended emission lines are identified. Bottom: Spectrum of RW Aur A, lightly-binned to a minimum of 2 counts per bin to show faint emission (22 counts) below 0.5 keV. The spectrum was extracted from a rectangular slit region of length 10" and full-width 0.8" oriented along the optical jet axes at P.A. =  $130^{\circ}/310^{\circ}$  and centered on the star.

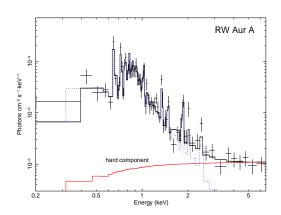


Fig. 5.— Unfolded spectrum of RW Aur A showing a fit (solid black line) with a 1T apec+ power-law (PL) model (Table 3). The thermal apec model (dashed blue line) reproduces the emission below  $\approx 2.5$  keV and the PL model (solid red line) accounts for the hard emission at higher energies. The hard component can also be reproduced using a very hot thermal plasma model (2T model in Table 3). The spectrum contains 986 counts (0.2 - 8 keV) of which 136 counts are in the hard 2 - 8 keV range.